EXPERIMENTAL STUDY OF ACOUSTIC ULTRA–HIGH-ENERGY NEUTRINO DETECTION

J. Vandenbroucke,[1] G. Gratta, and N. Lehtinen[2]

Physics Department, Stanford University, Stanford, CA 94305

ABSTRACT

An existing array of underwater, large-bandwidth acoustic sensors has been used to study the detection of ultra–high-energy (UHE) neutrinos in cosmic rays. Acoustic data from a subset of seven hydrophones located at a depth of ∼1600 m have been acquired for a total live time of 195 days. For the first time, a large sample of acoustic background events has been studied for the purpose of extracting signals from super-EeV showers. As a test of the technique, an upper limit for the flux of UHE neutrinos is presented, along with considerations relevant to the design of an acoustic array optimized for neutrino detection.

Subject headings: cosmic rays — neutrinos

1. INTRODUCTION

The detection of a neutrino component in cosmic rays above 10^{19} eV is a central goal of particle astrophysics. It is generally believed (Greisen 1966; Zatsepin & Kuzmin 1966) that the flux of cosmic-ray protons should drop sharply ("GZK" cutoff) between 10^{19} and 10^{20} eV because of pion photoproduction on the microwave background. Recent measurements using the Akeno Giant Air Shower Array (AGASA; Takeda et al. 1999) and the High Resolution Fly's Eye (HiRes) air fluorescence telescope (Abbasi et al. 2004) seem to disagree on the existence of such a cutoff, although it has been pointed out (Bahcall & Waxman 2003) that they may actually be consistent with one another. Neutrinos are likely to be an important component of the particle flux at ultrahigh energies. If the GZK mechanism is indeed present, the flux of ultra–high-energy (UHE) protons must be accompanied by UHE neutrinos ("GZK" neutrinos) from pion decay. Their clear detection would provide crucial input to the field.

Detection of the very small flux of cosmic rays at these extreme energies requires detectors of unprecedented size. Therefore, only detectors employing naturally occurring media are practical. The parallel development of several different techniques, some of which would ideally employ the same medium, is therefore crucial to constraining the measurements and providing sufficiently accurate and redundant information in order to fully understand cosmic rays at the highest energies. Indeed, in the last few years, great progress has been made in the use of radio signals for the detection of protons and neutrinos using a variety of natural targets, including lunar regolith (Gorham et al. 2004) and ice with ground-based (Kravchenko et al. 2003) and space-based (Lehtinen et al. 2004) antennas.

In this paper we describe the first experimental results obtained with the acoustic technique in ocean water. The possibility of acoustic detection of high-energy particles was first discussed in 1957 (Askar'yan 1957; Askar'yan & Dolgoshein 1977). Following this work, an extensive theoretical analysis of the processes relevant to signal formation was performed (Learned 1979), and the general phenomenon was confirmed with an accelerator test beam (Sulak et al. 1979). The first description of the properties of a practical, large array for UHE neutrino detection was given in Lehtinen et al. (2002). The dominant sound production mechanism, for nonzero water expansivity, consists of water heating in the region where a shower develops (instantaneously, from the point of view of acoustics), followed by expansion, producing a pressure wave. Only primaries that penetrate the atmosphere without interacting and then shower in the water are capable of producing detectable acoustic pulses, providing automatic particle identification within a broad range of energies. Acoustic sensor arrays can be substantially more sparse than optical Cerenkov arrays in water or ice because of the large (≈1 km) attenuation length of sound in water at the frequencies (≈10 kHz) where, for these events, most of the energy lies. However, as stressed in Lehtinen et al. (2002), the elongated shape of the showers produces acoustic interference that results in most of the sound emitted in a pancake-shaped volume with an opening angle of a few degrees. This effect is important for the optimization of a detector, since the optimal density of hydrophones is constrained by the ability to intercept these relatively narrow pancakes. Finally, the acoustic technique lends itself well to a calorimetric measurement of the total energy and would complement other technologies well.

2. THE DETECTOR

The Study of Acoustic Ultra–High-Energy Neutrino Detection (SAUND)[3] employs a large (∼250 km^2) hydrophone array in the US Navy Atlantic Undersea Test and Evaluation Center (AUTEC).[4] The array is located in the Tongue of the Ocean, a deep tract of sea in the Bahama islands at approximately N24°30′ and W77°40′. A detailed description of the entire array is given in Lehtinen et al. (2002). For the present work, we use a subset of seven hydrophones from the large array, arranged in a hexagonal pattern as shown in Figure 1. The hydrophones are mounted on 4.5 m booms standing vertically on the ocean floor. The horizontal spacing between central and peripheral hydrophones is between 1.50 and 1.57 km. The ocean floor is fairly flat over the entire array region, with our phones located at depths between 1570 and 1600 m. The hydrophones and their

---

[1] Currently at the University of California, Berkeley.
[2] Currently at the University of Hawaii, Manoa.
[3] See http://hep.stanford.edu/neutrino/SAUND.
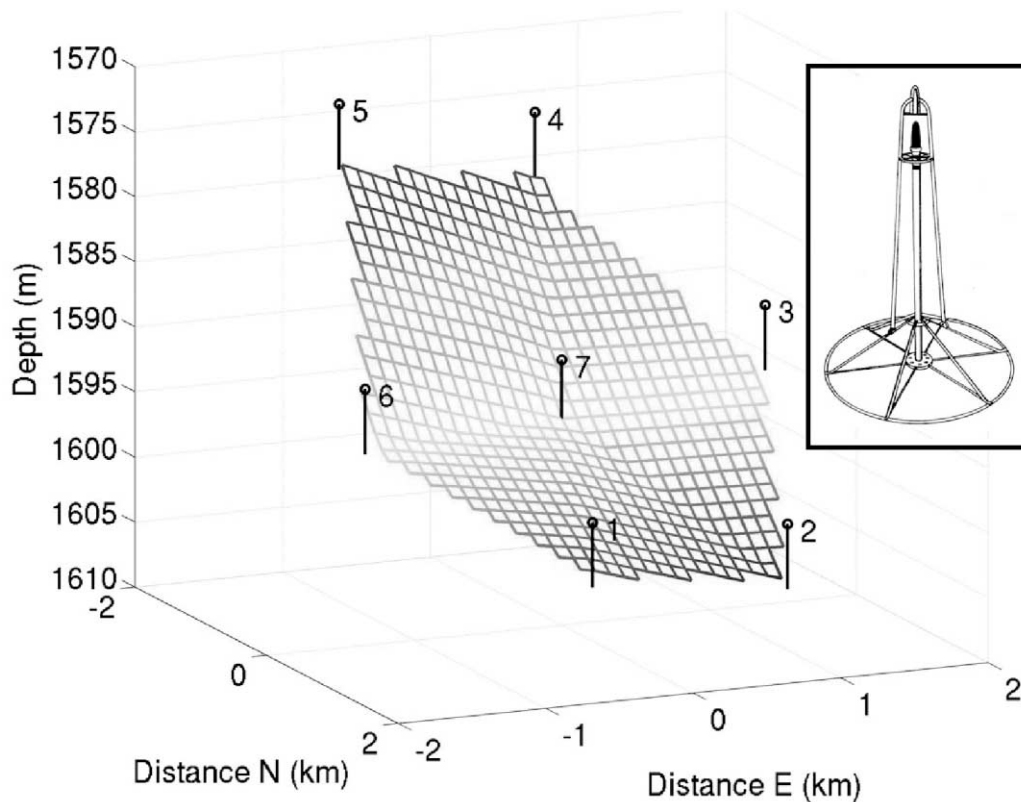[4] See http://www.npt.nuwc.navy.mil/autec.

FIG. 1.—Schematic view of the subset of hydrophones used for this work. The hydrophone depths are known precisely, while the sea-floor bathymetry between phones is estimated with a linear interpolation. The inset shows the 4.5 m tall hydrophone deployment and support structure. The bail used to deploy the phone folds and lies on the ocean floor during operation.

underwater preamplifiers have been in stable operation for naval exercises since 1969.

Analog signals are amplified at the hydrophones and fed through an onshore amplifier stage to a digitizer card[5] that continuously samples each of the seven channels at 179 ksamples s^{-1}. The time series in each channel is then fed to a digital matched filter implemented on a 1.7 MHz Pentium-4 workstation.

UHE neutrinos interact with matter by deep inelastic scattering on quarks inside nuclei. With increasing energy, the interaction cross section (Kwiecinski et al. 1999), and hence the probability of a neutrino interacting within the ocean water (which is thinner than the $\sim$100 km interaction length at 10^{21} eV), increases. After the primary interaction, the neutrino energy is distributed between a quark and a lepton. On average, the lepton acquires $\sim$80% of the energy (Gandhi et al. 1998). The remaining energy is dumped into the water as a hadronic shower aligned with the direction of the primary neutrino. The water is heated locally, causing it to expand and emit an acoustic pulse propagating perpendicular to the shower axis.

While a μ or τ neutrino generates only a hadronic shower, an electron neutrino also generates an electromagnetic shower, which is superposed on the hadronic one. However, because of the Landau-Pomeranchuk-Migdal (LPM) effect (Landau & Pomeranchuk 1953a, 1953b; Migdal 1956, 1957), the electromagnetic shower is elongated and has an irregular structure, producing weaker acoustic signals with irregular geometries. Here we only consider the hadronic showers, which exhibit the same structure for all kinds of neutrinos and are simulated with a simple parameterization following Alvarez-Muniz & Zas

(1998). This model includes π_0 interactions and the LPM effect for the electromagnetic components of the hadronic shower. Once the energy deposition has been determined using this shower model, the resulting acoustic pulse shape is simulated, following Learned (1979) and Lehtinen et al. (2002), at arbitrary positions (r, θ) with respect to the shower. As shown in Figure 2 for a fixed radial distance from the shower, the bipolar pulse is tallest and narrowest in a plane perpendicular
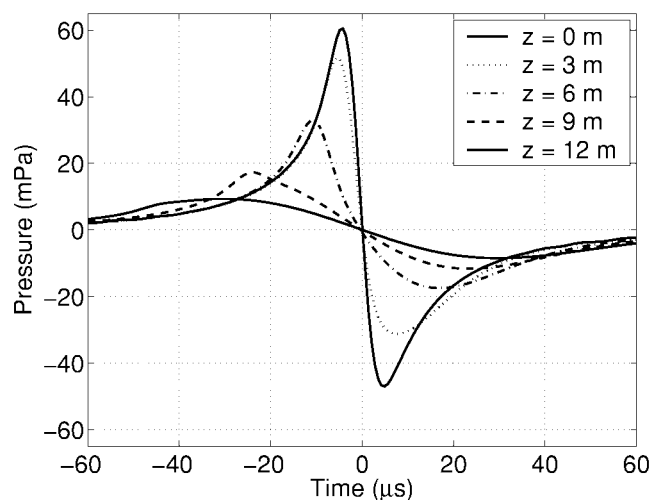

FIG. 2.—Simulated acoustic signals due to a hadronic shower of energy 10^{20} eV, corresponding to an initial neutrino energy of 5×10^{20} eV. Signals are shown at 1050 m distance perpendicular to the neutrino path. The five different curves refer to longitudinal distances of 0, 3, 6, 9, and 12 m forward from the shower maximum.

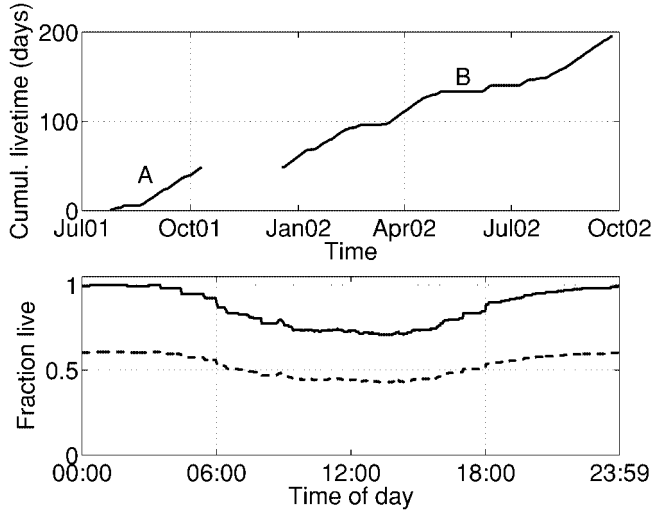[5] National Instruments Model PCI MIO 16E1.

Fig. 3.—Live time for SAUND. *Top*: Data accumulation as a function of time. A test run (run A, 48 days), not used in the present analysis, was followed by a system upgrade and a longer period of stable running (run B, 147 days). *Bottom*: Solid curve gives the fraction live as a function of time of day, for days during which any SAUND run B data were collected. The dashed curve represents the data used for the analysis reported here, and it includes down time from bad weather and hardware failures.

to the shower axis, at the longitudinal location of the shower maximum.[6] The pulse becomes shorter and wider at greater longitudinal distances from the maximum. The general features of the pulse shape match the data from Sulak et al. (1979).

Triggering is achieved in SAUND with a digital matched filter that searches for signals matching the expected neutrino signal, appropriately weighting frequency components according to their signal-to-noise ratio (Hogg & Craig 1995). The filter response function is obtained by transforming to the frequency domain the expected signal shape, which is approximated in the time domain by the analytical form $S(t) \propto -(t/\tau)e^{-t^2/2\tau^2}$. The characteristic time of the signal depends on position (r, θ) relative to the shower (see Fig. 2). A characteristic time of $\tau = 10$ μs, corresponding to the width of the largest expected signals, is chosen for the present work. To obtain the filter transfer function, the expected signal in the frequency domain, $\tilde{S}(f)$, is divided by the noise spectrum, assumed to be of the Knudsen type (Knudsen et al. 1948): $\tilde{N}(f) \propto f^{-\alpha}$. The expected $\alpha = 1.7$ is approximated with $\alpha = 2$ for analytical convenience. The transfer function $\tilde{H} \propto \tilde{S}(f)/\tilde{N}(f)$ is then transformed to the time domain to obtain the response function:

$$H(t) = \left[\left(\frac{t}{\tau}\right)^3 - 3\left(\frac{t}{\tau}\right) \right] e^{-t^2/2\tau^2}. \quad (1)$$

Each channel is continuously filtered, and the filter output is compared to a threshold. The filter is implemented with a discretized version of the above response function, sampled at the same frequency as the pressure waveforms (179 kHz); 12

samples ranging from $t = -30.8$ to $t = 30.8$ μs are used. Beyond this range, the response function is below 13% of its peak amplitude. When the threshold is exceeded, a trigger occurs and event data are recorded.

Signals from the highest energy neutrinos considered here are expected to saturate the digitizer, and ~10% of the waveforms in the data set are saturated. By simulating the effects of saturation on the digital filter and on subsequent offline cuts, we found that saturation does not pose a problem for the present analysis. This is because the cuts rely primarily on frequency and timing information, not on amplitude.

By arrangement with the US Navy, the SAUND data acquisition system (DAQ) is connected to the hydrophone array only when the array is not in use for Navy exercises. The live time achieved under this agreement is shown in Figure 3. As shown in the top panel, a test run (run A) was used to commission the system and is not used for the present analysis. The system was upgraded from 2001 October to 2001 December and run for an integrated 147 days live with stable conditions (run B). Only this stable run is used for the analysis presented here. The solid curve in the bottom panel shows the live time achieved at different times of day. The live time is close to 100% at night, when no Navy tests are conducted, and it drops to about 70% in the middle of the day. The average over a day is 86%. In addition, an overall live-time reduction due to weather conditions and hardware failures resulted in the dashed line in the bottom panel of Figure 3.

Because the noise environment is volatile, an adaptive trigger threshold is used. Every minute the threshold is raised or lowered based on whether the number of events in the previous minute was above or below the target rate of 60 events minute^{-1}. Events are accumulated in memory each minute and written to disk, along with data relevant to the entire minute, at the end of the minute. The distribution of thresholds in run B is shown in Figure 4. To simplify online processing and offline event reconstruction, the threshold value is constrained to discrete values (integer multiples of 0.004, in units of digital filter output). For the purpose of neutrino analysis, only thresholds
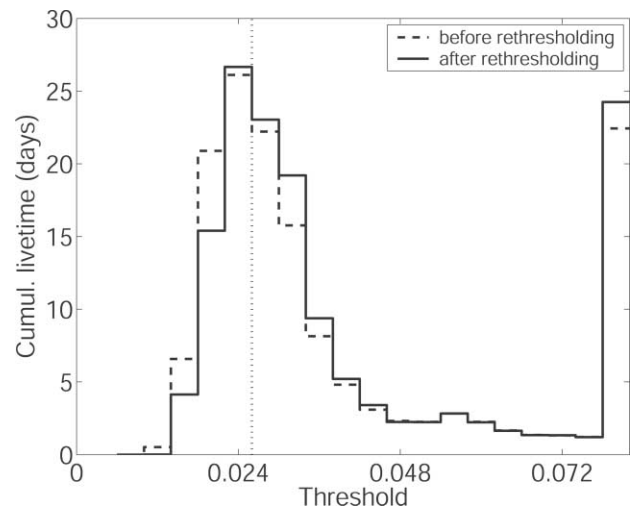

Fig. 4.—Integrated live time at each discrete threshold. The distribution has a long tail extending beyond the range shown here; this tail has been added to the last bin of the figure. The threshold step size is 0.004. The four values from 0.012 to 0.024 (left of the vertical line) are considered quiet and used for the present analysis. Including data taken at larger thresholds would increase the background while negligibly increasing neutrino exposure. The dashed and solid histograms represent the same quantity before and after, respectively, the offline rethresholding described in the text.

---

[6] We note here that an erroneous value for the volume expansivity of seawater was used in Lehtinen et al. (2002). A value of 1.2×10^{-3} was used instead of the correct value of 0.15×10^{-3}. This resulted in a simulated signal amplitude larger than the correct value by a factor of 8. This error is corrected in the present work.

between 0.012 and 0.024 are used. These "quiet" periods account for 37% of run B.

In total, run B contains 20 million triggers (250 GB) corresponding to $\sim$1.7 GB day^{-1}. Every few weeks, data are transferred to an external hard drive that is shipped to Stanford for offline analysis. Nine-tenths of the triggers are captured for 1 ms; one-tenth are captured for 10 ms in order to record and study reflections from the ocean bottom.

The frequency response of the hydrophone/amplifiers chain is flat to better than 8 dB between 7.5 and 50 kHz. A sharp cutoff of 100 dB/octave below 7.5 kHz is due to an analog high-pass filter in the system, while a somewhat slower rolloff, due to the sensor itself, occurs above 50 kHz. The low-frequency cutoff, while not ideal for neutrino detection, is not a significant hindrance.

The phase response of the hydrophone/amplifiers chain is difficult to measure and at present is not well known. In order to gain some quantitative understanding of its possible effects on the trigger, the efficiency of the filter was calculated for the pulse shapes in Figure 2 and for their first and second time derivatives, after applying a ninth-order Butterworth bandpass filter to mimic the AUTEC frequency response. For each of these phase responses, efficiency was calculated as a function of energy. The resulting trigger thresholds have a spread of a factor of 2 for any given energy. Conservatively, the highest of these thresholds is assumed in the present analysis.

In addition to the matched filter described above, an online veto is applied to remove a specific kind of noise that is time-correlated in all channels. This noise consists of simultaneous sinusoids in all seven channels, occurring in bursts with a 60 Hz repetition rate. While the origin of these signals is unknown, it is clear that they originate from electrical pickup, because the sound velocity does not allow for simultaneous, correlated acoustic events in all phones. The veto removes this noise by rejecting events with large seven-channel pairwise correlation,

$$C = \sum_{i<j} \sum_{t} p_i(t)p_j(t), \qquad (2)$$

where the time sum is taken over discrete samples and p_i is the pressure time series at phone i, normalized by mean absolute amplitude: $p_i = P_i/\langle|P_i|\rangle$, where P_i is the absolute pressure and $\langle|P_i|\rangle$ is its average over the captured waveform. Events with $C > 500$ are removed.

Every 10 minutes, time series for all channels are collected for 100 ms in forced mode. These data are used for offline noise analysis and for simulating the noise conditions in our efficiency calculation. Every minute the noise spectrum is calculated from a 100 ms long time series. A typical noise spectrum is given in Figure 5.

SAUND run B provides the largest data set ever collected for the purpose of studying acoustic techniques in UHE particle detection. During the run it has been our strategy to collect data with consistent and stable conditions for an extended period of time. A number of improvements in trigger efficiency, stability, and uniformity have been developed from run B and will be implemented in future runs.

3. ENERGY AND POSITION CALIBRATION

Small implosions are useful calibration sources for underwater acoustics. Household light bulbs, which implode at a particular failure pressure while sinking, releasing energies of
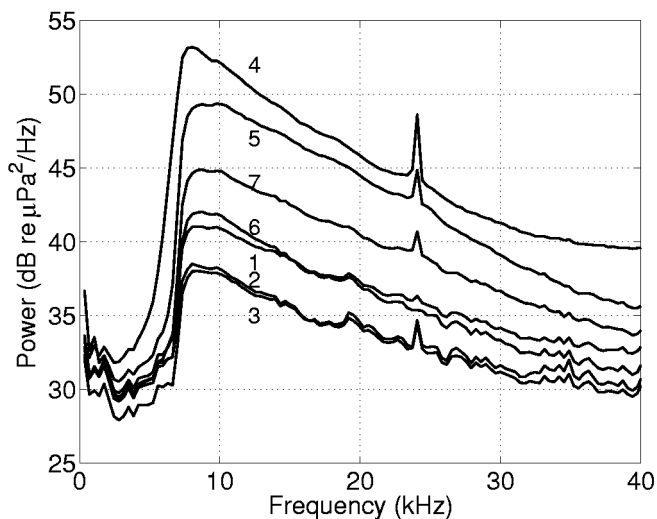

Fig. 5.—Typical average noise spectrum as measured by SAUND in run B. The plot shows the spectrum averaged over 10 hr from midnight to 10:00 A.M. on 2001 December 22. The range of noise levels is mainly due to variations in amplifier gains. Note the 7.5 kHz high-pass filter and the $\sim$24 kHz peak from a transmitter used by the Navy. The sea state noise dominates these spectra.

order 100 J,[7] are a particularly convenient source (Heard et al. 1997). A calibration run of this type was performed on the morning of 2001 July 30 (at the beginning of run A).

The small boat used for the calibration was positioned over the central hydrophone using a handheld Global Positioning System (GPS) receiver.[8] The boat engine was then turned off and several light bulbs were sunk as the vessel drifted for about 30 minutes. Two more GPS fixes were acquired during the calibration.

The waveforms recorded for one of the implosion events are shown in Figure 6. The first pulse corresponds to the direct acoustic signal arriving at the central hydrophone. The pulse around 0.2 s corresponds to the arrival at the hydrophone of the signal reflected by the surface of the ocean. Direct pulses in all other six hydrophones appear between 0.4 and 0.5 s, followed in turn by the respective surface reflections. In Figure 7 the waveform for the central hydrophone is shown on an expanded timescale, clearly showing the bottom reflection around 6 ms.

Also shown in Figure 7 is the structure of the direct pulse. The signal is expected to be a damped sinusoid, generated by the "breathing" oscillations of the gas bubble produced by the bulb. In our case, the primary resonant frequency of the bubble, at a depth of 100–200 m, is predicted to be 700–1300 Hz (Heard et al. 1997). The signal shown in Figure 7 shows a second peak at about 1 ms, confirming this prediction. The measured waveform is consistent with the predicted waveform after a 7.5 kHz high-pass filter.

A time difference of arrival (TDOA; Spiesberger 2001) analysis can be used to reconstruct the three-dimensional location of acoustic events. This method uses only timing information. In a homogeneous medium, the difference in arrival times between each pair of hydrophones constrains the source location to a hyperboloid. Four hydrophones (three independent time differences) are necessary to determine three hyperboloids, the

---

[7] For the most common household ("A19" sized) incandescence bulbs ($\sim$6.7 cm diameter); no signal was detected from miniaturized bulbs ($\sim$1 cm diameter), possibly because no implosion occurs.
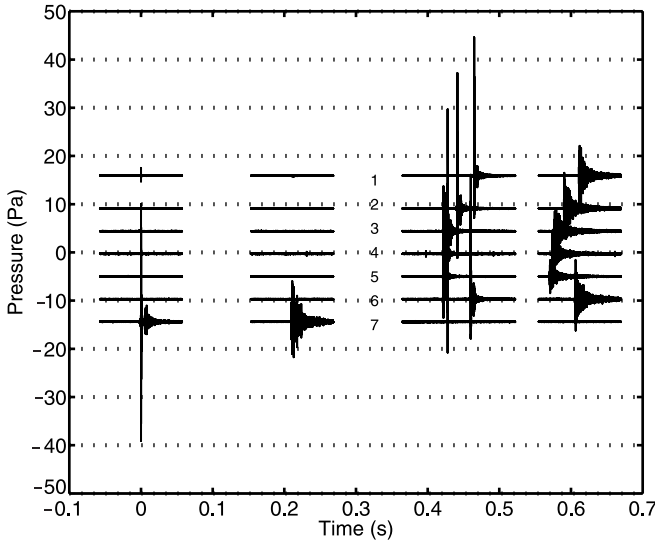
[8] Magellan, model 310.

FIG. 6.—Signals from a light bulb implosion. Time series from all seven hydrophones are shown. A direct signal at the central hydrophone is immediately followed by a bottom reflection and, much later, by the signal from the reflection off the ocean surface. Similar sets of three signals appear, at a later time, on the surrounding six hydrophones. The signals in different channels are displaced vertically for clarity. The small signal in phone 1 at $t = 0$ is electrical cross talk due to the large signal in phone 7.

intersection of which can be found analytically and generally results in two points. For our sea-floor, planar array, the two solutions are usually symmetric about the detector plane, and the solution below the sea floor can be discarded.

While an analytical TDOA solution is possible in homogeneous media, the ocean is not homogeneous but is a layered medium. At AUTEC, the sound velocity varies with depth, as shown in Figure 8. This results in sound-ray refraction, as illustrated in the same figure. Over the fiducial volume of the SAUND detector, refraction significantly affects position reconstruction. The effect warps the TDOA hyperboloids, mak-
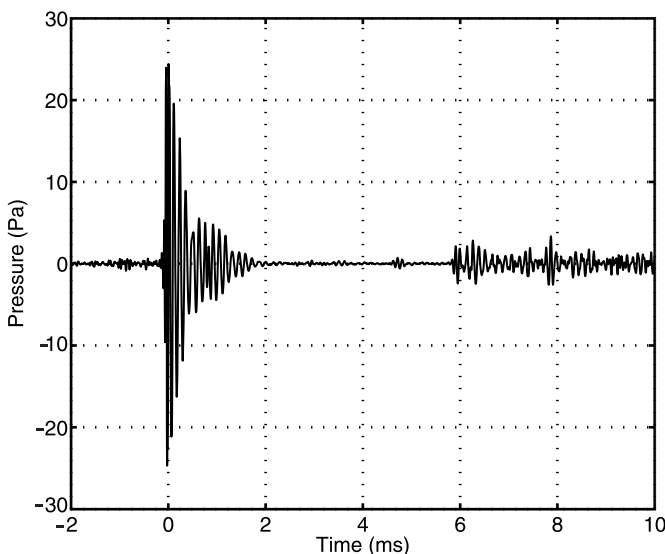

FIG. 7.—Detail of the light bulb implosion signal at the central hydrophone. Both the direct signal and, after a 6 ms delay, the bottom reflection, are evident. The oscillations in the envelope of the direct signal are due to a combination of the bubble rebound from the implosion (Heard et al. 1997) and the response of the hydrophone, cable, and amplifiers.
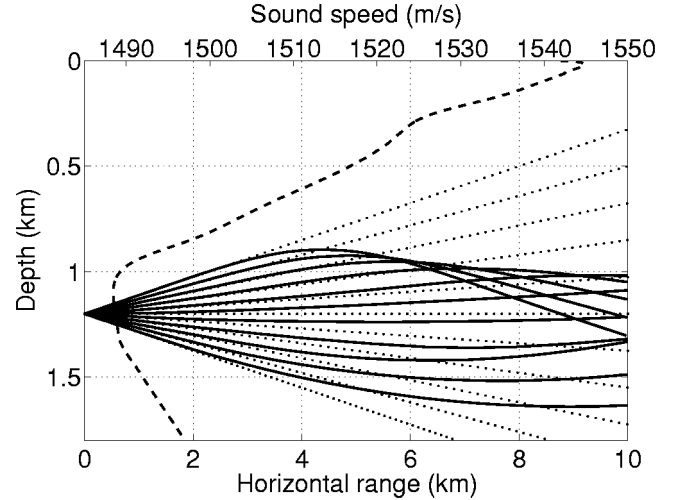

FIG. 8.—Example of ray trace showing the effects of refraction. Eleven rays are emitted from a source at 1200 m depth, from $5°$ below to $5°$ above the horizontal. Refracted (*solid lines*) and unrefracted (*dotted lines*) rays are plotted together for comparison. For reference, the sound speed as a function of depth (sound velocity profile; SVP), used to calculate the ray trace, is also shown (*dashed line*).

ing an analytical solution impossible. A numerical solution is sought by minimizing the metric

$$m(s) = \frac{1}{N-1} \sum_{i<j} \left[t_{ij}^{\text{meas}} - t_{ij}(s) \right]^2 \tag{3}$$

with respect to s, the test location for the acoustic source. Here t_{ij}^{meas} is the measured TDOA between phones i and j ($t_{ij}^{\text{meas}} = t_i^{\text{meas}} - t_j^{\text{meas}}$) and $t_{ij}(s)$ is the theoretical difference in arrival times for a source at s [$t_{ij}(s) = t_i(s) - t_j(s)$]. For N phones recording a signal, the sum occurs over the $N-1$ independent pairs of arrival time differences.

The theoretical travel time from the test source location to phone i, $t_i(s)$, is calculated using a ray-trace algorithm that divides the water into layers in each of which the sound speed is a linear function of depth. The ray follows the arc of a circle within each layer (Boyles 1984). Practically, the ray trace is too time intensive to be performed for each test source location. For each phone, a table of travel times from points on a grid spanning the detector volume to the phone is built. The minimization begins at the best grid point, and the grid is linearly interpolated to find the off-grid source location. The grid is built once, and the interpolation then occurs for each event reconstruction. While the local sound velocity profile (SVP) is measured almost daily by the Navy and is available to us, it was found that seasonal SVP variations introduce errors smaller than those due to the uncertainty in the hydrophone location. Hence a single table built from an average SVP is used for all reconstructions. The position reconstruction algorithm takes a few seconds to run, for each localization, on a 1.6 GHz Athlon CPU (offline computer).

Because the light bulb implosions are far above noise, their TDOA localization is performed using all seven direct signals (six independent time differences), rather than five, as used for events triggered in neutrino mode. The reconstructed depth of bulb failure, D, is then used to estimate the energy released in the implosion, $P_{\text{amb}}V$. Here $P_{\text{amb}} = \rho g D$ is the ambient pressure at the reconstructed implosion depth, ρ is the approximate density of sea water ($\rho = 1$ g cm^{-3}), g is the acceleration due
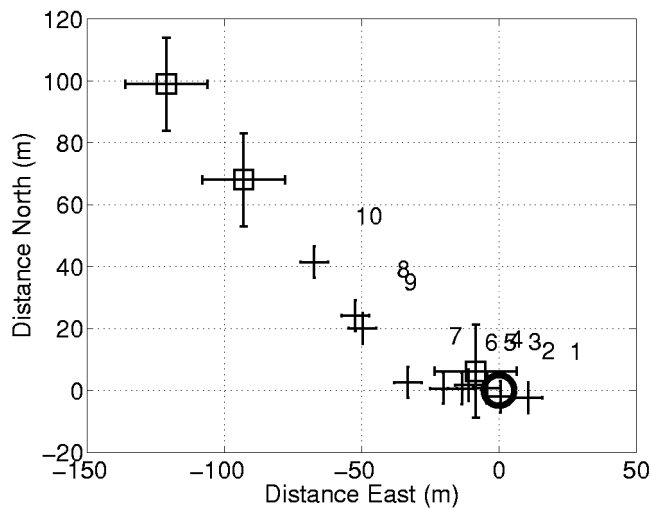
Fig. 9.—Trail of implosions of bulbs dropped from a drifting boat, as reconstructed from TDOAs. The reconstructed positions are indicated by crosses, with bulb labels offset for clarity. The boat's motor was cut after starting approximately above the central hydrophone (marked by a circle). The larger crosses represent the boat positions measured at three times with the GPS device. Bulbs are numbered by the order in which they were dropped. The bulb drop spanned $\frac{1}{2}$ hr.

TABLE 1
PARAMETERS OF THE IMPLOSION CALIBRATION EVENTS

Bulb (1)	D (m) (2)	P_{amb} (kPa) (3)	$P_{amb}V$ (J) (4)	E_{theor} (J) (5)	E_{det} (J) (6)
1.........................	170	1640	250	3.1	1.7
2.........................	110	1120	170	1.9	0.3
3.........................	150	1430	210	2.6	1.5
4.........................	170	1690	250	3.2	2.8
5.........................	130	1300	200	2.3	0.8
6.........................	110	1050	160	1.8	0.4
7.........................	90	900	140	1.5	0.1
8.........................	140	1380	210	2.5	1.9
9.........................	200	1930	290	3.8	1.9
10.......................	300	2930	440	6.7	1.8

NOTES.—D is the reconstructed implosion depth and $P_{amb} = \rho g D$ is the ambient pressure at D. Here $\rho \simeq 1$ g cm^{-3} is the density of sea water and $P_{amb}V$ is the implosion energy, with $V = 150$ cm^3 as the bulb volume. The expression E_{theor} is the theoretical detectable acoustic energy, assuming 4% conversion of the energy $P_{amb}V$, as appropriate for implosions triggered with a hammer device (Heard et al. 1997); E_{theor} includes the effects of absorption and SAUND's frequency response. The somewhat lower yield observed (E_{det}) is consistent with the expectation of lower acoustic coupling for implosions allowed to occur at failure pressure rather than forced at lower pressure with a hammer device (Heard et al. 1997).

to gravity, and $V \sim 150$ cm^3 is the volume of the light bulb. From our position reconstruction P_{amb} is found to be of order 1000 kPa, while the internal pressure of the bulbs is believed to be slightly below one atmosphere (70–90 kPa; Heard et al. 1997). The total acoustic energy detected at phone i, $E_{det}(i)$, can be calculated independently assuming spherical emission (Elmore & Heald 1986):

$$E_{det}(i) = \frac{4\pi r^2}{\rho c} \int P^2(i,\ t)\, dt, \qquad (4)$$

where $P(i,t)$ is the recorded pressure time series at phone i and r is the distance from phone to reconstructed implosion location. Lensing effects due to the changing sound velocity as a function of depth were studied and found to be negligible for these source locations.

The horizontal reconstructed positions of the light bulb implosions are shown in Figure 9, along with the three GPS fixes of the boat from which they were dropped. The implosions are sequentially numbered in the order in which they occurred. The GPS points, shown with the ±15 m errors quoted by the specifications of the instrument, are in good agreement with the TDOA reconstruction. The extent of the drift is consistent with a current of about 5 cm s^{-1} (0.1 knot).

The results of depth and energy reconstruction for the implosions are shown in Table 1. The uncertainty of position reconstruction near the surface directly above the center of the array (the optimal location for source localization) is 5 m. The implosion pressures P_{amb} are consistent with the literature (Heard et al. 1997). The efficiency of conversion from $P_{amb}V$ to acoustic energy is expected to be about 4% (Heard et al. 1997). In addition, the acoustic frequency spectrum from the implosion is known to be peaked around the air bubble resonant frequency of ~1 kHz, well below AUTEC's low-frequency cutoff (Gaitan et al. 1992; Keller & Kolodner 1956; Keller & Miksis 1980), so that only about one-half of the acoustic energy lies within AUTEC's bandwidth. The expected energy, taking into account both the 4% yield and the bandwidth mismatch, is

shown in column (5) of Table 1. From energy reconstructed using recorded amplitudes (col. [6]), we find that the yield is in practice somewhat lower and that it fluctuates substantially from one event to another. Both these effects are possibly due to the fact that the bulbs are allowed to implode at failure pressure rather than being intentionally broken at lower ambient pressure (Heard et al. 1997).

4. DATA REDUCTION

The online trigger system is designed to select impulsive bipolar signals while rejecting most of the Gaussian noise. Because of the novelty of the technique, trigger conditions are chosen to be rather loose and substantial background is left to be rejected by offline analysis. Impulsive backgrounds to UHE showers are expected to arise from a variety of human and nonhuman sources. In particular a number of animals, from large cetaceans to small crustaceans, are known to produce high-frequency acoustic transient noises. While the Tongue of the Ocean is relatively isolated from the open ocean and hence rather quiet, an important motivation for this first large-volume data-taking campaign is the exploration of such coherent backgrounds.

Offline data reduction is used to select events consistent with neutrino-induced showers while rejecting backgrounds in SAUND run B. The efficiency of each step of data reduction is estimated using simulated neutrino events to which, as discussed above, bandpass filtering is applied to account for the known frequency response of the array. As is also described above, the unknown phase response of SAUND is addressed by repeating the efficiency analysis with the first and second derivative of the simulated and filtered signal. The worst case (lowest efficiency) is then assumed. The overall efficiency of the data reduction cuts is greater than 0.87 and is approximated as 1. The data reduction power of each analysis cut is shown in Table 2.

The first step in offline data analysis is a set of data quality cuts. These are particularly important because of the volatility of the background noise. The adaptive thresholding algorithm used online was in some cases found to be too slow in

TABLE 2

EVENT RATES

Cut/Description	Events
1. Online triggers:	
a) Digital filter	64.6 M
b) Correlated noise	20.2 M
2. Quality cuts:	
a) Offline rethresholding	7.23 M
b) Offline quiet conditions	2.60 M
c) $\Delta t_0 > 1$ ms	2.56 M
3. Waveform analysis:	
a) Remove spikes	2.03 M
b) Remove diamonds	1.96 M
c) $f_e > 25$ kHz	1.92 M
4. Coincidence building:	
a) Coincidence	948
b) Localization convergence	79
5. Geometric fiducial region	0

NOTES.—Event rates at different stages of online (1) and offline (2–5) data reduction. Note that the cuts in 1–3 are applied to single-phone events, while the cuts in 4 are applied to coincidences between five phones. The ''Events'' column gives the number of events surviving a particular cut and all the preceding ones. Cut 4*a* includes both coincidence windowing and hit-phone geometry (requiring the set of five hit phones to be one of the six trapezoidal configurations). Finally, Cut 5 requires the sources to be in the geometric region consistent with neutrino showers, and it eliminates all remaining events.

reacting to the changing conditions. Hence, offline rethresholding is applied by raising the threshold whenever the rate exceeds 60 events minute^{-1} (see Fig. 4). The cut selecting quiet events is applied using the threshold values after rethresholding. Finally, events with $\Delta t_0 < 1$ ms are removed, where Δt_0 is the difference in time stamps between the current event and the previous one. This last cut rejects bursts of events that occasionally occur when the threshold has not adapted sufficiently and is too low. The combination of all event quality cuts reduced the run B data set from 20.2 to 2.56 million events, with an estimated neutrino efficiency of more than 99% (counting the quiet cut as a live-time reduction, not an efficiency reduction).

Waveform analysis is then used to further reduce the background. A powerful method of event classification is provided by the scatter plot between effective frequency f_e and duration, measured in effective number of cycles n_e. We define the effective frequency as

$$ f_e = \frac{1}{2\pi\Delta t} \cos^{-1}\left[\frac{\langle P(t)P(t+\Delta t)\rangle}{\langle P^2(t)\rangle}\right], \qquad (5) $$

where $P(t)$ is the recorded pressure time series and Δt is the sampling time (5.6 μs), which is small compared to the signal
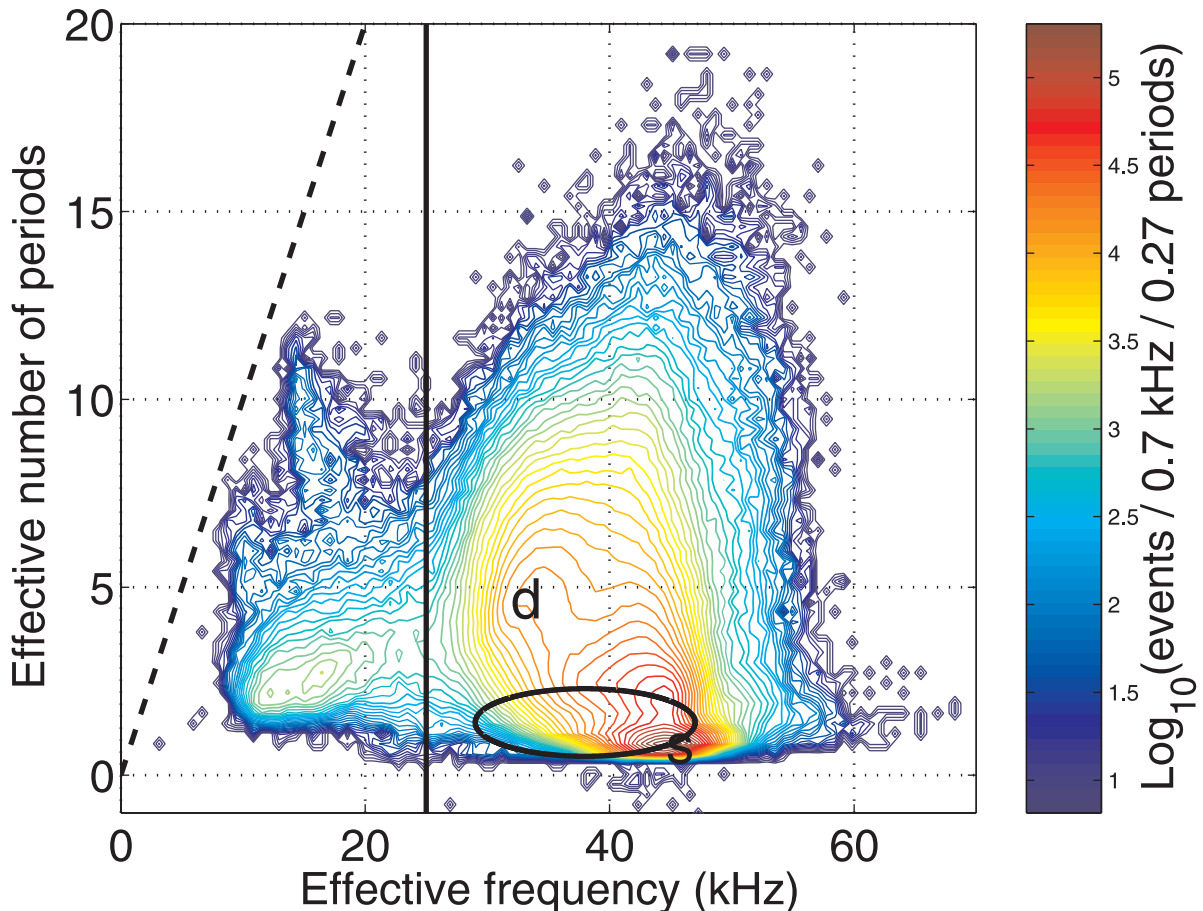

FIG. 10.—Contour plot between effective frequency and effective number of periods, as defined in the text. The dashed line represents an upper bound due to the finite length of the capture window (1 ms). The events clustered near this line are due to Navy pingers at specific frequencies. The solid vertical line indicates a cut discussed in the text. The ellipse indicates the envelope of approximate locations of the simulated neutrino events with different combinations of filtering and differentiation as discussed in the text. The letters s and d identify regions where spike- and diamond-type events cluster.

oscillation period. The effective duration in number of cycles is given by $n_e = D_e f_e$, where

$$D_e = \frac{E_S}{(1/2)P_{peak}^2} \qquad (6)$$

is the duration of the signal in units of time. Here P_{peak} is the maximum absolute amplitude of the recorded time series and

$$E_S = E_{S+N} - E_N = \int P^2(t)\, dt - \int P_{rms}^2\, dt, \qquad (7)$$

where P_{rms} is determined from the noise spectrum calculated once per minute. The normalization is such that a sinusoid, in the limit of many periods in the capture window, will give n_e equal to the number of cycles of the sinusoid. The contour plot between these two parameters is shown in Figure 10 for the 2.56 million events left in the data set. Also shown in Figure 10 is the envelope of the regions containing ~95% of the neutrinos simulated, filtered, and differentiated as described above.

The general region marked "s" in the contour plot includes events, here called "spikes," in which a single digital sample is displaced from the rest of the waveform. Spike events occurred in bursts with a 50 Hz rate and ceased when a large radar system near our DAQ system was disabled. We reject spike events with the metric

$$m_{spike} = \frac{M_1(|P|) - M_2(|P|)}{M_1(|P|)}, \qquad (8)$$

where P is the pressure time series and M_1 and M_2 give the largest and second largest amplitude samples, respectively. Events with $m_{spike} < 0.7$ are retained.

The region of Figure 10 marked "d" includes events, here called "diamonds," consisting of a diamond-shaped envelope containing many cycles. These events, an example of which is shown in the top panel of Figure 11, are believed to be genuine acoustic signals produced by marine mammals swimming in the area. They can be rejected with a digital matched filter whose response function was constructed by averaging 10 hand-picked examples of good diamond events. The diamond rejection metric, $m_{diamond}$, is defined for a given waveform to be the maximum output of this digital filter acting on the waveform. Events with $m_{diamond} < 0.7$ are retained.

Finally, neutrino candidates are required to have $f_e > 25$ kHz. This cut eliminates low-frequency noise originating from sources including marine mammals, boats, and AUTEC pingers.

Waveform analysis reduces the data set from 2.56 to 1.92 million events, retaining ~93% of the simulated neutrino events.

Coincidences between different hydrophones are reconstructed from the reduced data set. The reconstruction program first finds cases in which five different phones trigger within a 2.27 s coincidence window. This window is the maximum possible time delay between phones plus a 10% buffer to account for measurement errors and refraction. We then require that the five events satisfy causality pairwise, a more stringent requirement than the initial windowing, again with a 10% buffer. Finally, we apply a phone geometry cut: there are 21 ways to choose five of the seven phones. Six of these combinations, those forming a trapezoid, are consistent with a pancake radiation pattern triggering all phones enclosed by the pattern. Only coincidences triggering one of these six five-phone combinations are retained.
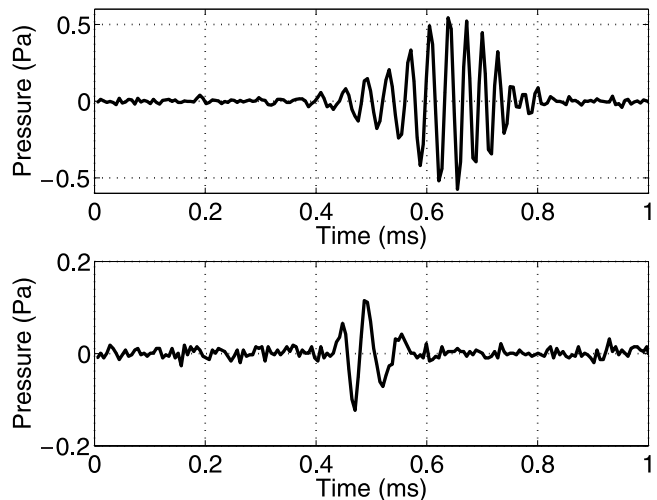

FIG. 11.—Waveforms of two important classes of background. *Top*: Diamond events. They are easily rejected with a digital matched filter. *Bottom*: Multipolars. Depending on the phase response of the SAUND detector, multipolar events could be indistinguishable from neutrino signals.

These timing and geometric cuts greatly reduce the data set, from 1.92 million to 948 events, retaining an efficiency of 95% for neutrino events. Such a substantial data reduction is essential in order to perform the computationally intensive origin localization with TDOA in a layered medium. A given single-phone trigger may be included in several (even many) five-trigger coincidences. This is because coincidence is a much less powerful requirement for acoustic signals than for electromagnetic signals, because the propagation speed is 2×10^5 times lower. While only four phones are required for TDOA localization, five-phone coincidence is demanded, both to overconstrain the reconstruction and to reduce the background, without significantly decreasing the neutrino efficiency.

For most coincidences, TDOA does not converge on a consistent solution to the causality equations (solved numerically, accounting for refraction with ray-trace tables). These coincidences are presumably accidental and are therefore discarded. Most of the 79 events remaining in our data set have "multipolar" waveforms at more than one of the five phones triggered. It is apparent that this class of events may be difficult to separate from genuine neutrino signals on the sole basis of pulse-shape properties. To explore the properties of multipolar events, we have built a digital matched filter using the average of 11 waveforms from events manually chosen as good examples of this event type. By applying the matched filter to earlier stages of the event selection, it was found that multipolar events tend to accumulate in periods of large adaptive threshold, and many such events in the original data set are rejected by the "quiet conditions" cut (2b in Table 2). Clearly a full pulse-shape calibration, including phase, of the acoustic sensors and their readout chain will be essential for future detector arrays. For the present data set we conservatively do *not* use the multipolar event digital filter. As we show in § 5, geometric considerations make all of these events inconsistent with a neutrino origin.

5. ACCEPTANCE ESTIMATE

The Monte Carlo (MC) simulation used to estimate the detector efficiency is run for a set of discrete primary neutrino
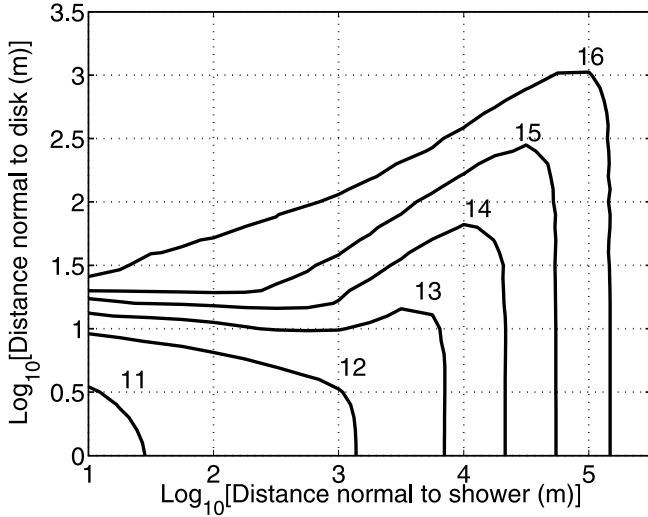
FIG. 12.—Neutrino detection contours for SAUND, for a trigger threshold of 0.02. In the plot the neutrino producing the shower propagates along the vertical axis. The shower maximum is at the origin of the coordinate system. Curves are labeled by $\log_{10}[E(\mathrm{GeV})]$. Only one quadrant is represented.

FIG. 13.—Effect of refraction on the acoustic radiation envelope (pancake). A cross section of the acoustic radiation pattern from a 3×10^{21} eV neutrino at $0°5$ zenith is shown with and without refraction. Projections of the seven hydrophone locations onto the cross sections are shown for reference. Note that the detector is inclined to $\sim 0°5$ zenith, $7°$ east of north because of the slightly sloping sea floor.

energies. For each energy, detection contours, examples of which are given in Figure 12, are calculated by determining the pressure pulse at each point in space (accounting for attenuation) and then applying the digital filter. For each energy $N_{\mathrm{MC}} = 10^5$ simulated neutrino events are produced with random orientations and positions in a water cylinder of radius 5 km, centered around the central phone. The detection contour is then "bent" to account for refraction and its intersection with the different phones in the array is tested as shown, for a particular configuration, in Figure 13. For an energy E the acceptance is then given by $A_i(E) = A_0 N_i / N_{\mathrm{MC}}$, where N_i is the number of Monte Carlo events producing five or more hits at the threshold value identified by i; $A_0 = \Omega_0 V_0$ is the acceptance that would result if all N_{MC} events were detected, where Ω_0 is the total solid angle, and V_0 is the total volume within which events are chosen.

Although the outer hydrophones are only 1.5 km from the central one, it was found that events with the appropriate orientation can safely be detected and localized up to a radial distance of 5 km. Outside of this region, however, the rays reach vertical turning points, and precise source localization becomes difficult. For this reason, we conservatively limit the fiducial volume to 5 km radius. The requirement that the radiation pancake intercepts several hydrophones almost coplanar with the sea floor forces the direction of the accepted neutrinos to be close to vertical.

The uncertainty in source position reconstruction, estimated from Monte Carlo data, worsens steadily with distance outside the array, but it does not exceed 500 m (vertical) and 200 m (horizontal) for radial distances smaller than 5 km. The positions of detectable neutrino Monte Carlo events with energies of 10^{14}, 10^{15}, and 10^{16} GeV are shown in a side (top) view in Figure 14 (Fig. 15). The concentration of events slightly above the plane defined by the phones is consistent with the geometric considerations above. The positions of the 79 acoustic events passing all analysis cuts (except for fiducial volume) in run B are also shown as small squares. There is a clear separation between these events, mainly concentrated in the water column above the hydrophones, and the region where the neutrino events are expected to be. Hence, we conclude that the
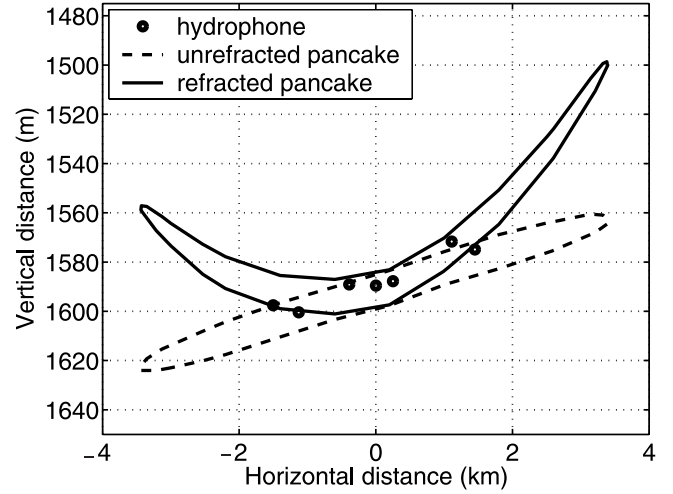
spatial distribution of the observed events is incompatible with the one expected from neutrino interactions. The expected pancake shape of the acoustic emission profile from neutrinos is an essential assumption of this assertion.

Focusing effects can potentially alter the detected energy and hence the threshold value. As shown in Figure 16, such focusing effects are small for sources in the neutrino fiducial volume and are neglected.

In order to express this result as an upper limit to the UHE neutrino flux, we define a fiducial volume given by the revolution of the dashed triangle around the vertical axis. The fiducial region is chosen to be slightly above the ocean floor in order not to be affected by floor roughness. Ideally, the fiducial volume choice would have been based entirely on the signal Monte Carlo events. However, given the novelty of the technique and the present emphasis on studying backgrounds, such a "blind" approach is impractical here. The separation between expected neutrino region and observed coincidences is nevertheless striking enough that the definition of the fiducial volume is unambiguous. In fact, the main source of uncertainty in our analysis lies in the assumptions made about the phase response of the array. No five-phone coincidences are present in SAUND run B within the fiducial volume.

From the geometric acceptance $A_i(E)$ defined above, a "neutrino exposure" $X_i(E) = A_i(E) N_A \sigma(E) T_i$ is computed. Here N_A is the Avogadro number, $\sigma(E)$ is the neutrino cross section, and T_i is the live time for a particular value of the adaptive threshold, labeled by i; σ is estimated by extrapolating the power-law fit given for energies between 10^{16} and 10^{21} eV (Gandhi et al. 1998). Fits for neutrinos are used, the antineutrino fits being very similar. Exposures collected at different thresholds are then added together. A 90% CL flux limit is then calculated following the method of Lehtinen et al. (2004) using Poisson's statistics and the fact that no events are observed. The resulting limit (multiplied by E^2, as customary) is shown in Figure 17 along with the limits already available from FORTE (Lehtinen et al. 2004), RICE (Kravchenko et al. 2003), and GLUE (Gorham et al. 2004), and with fluxes predicted by various theories (Weiler 2001; Gelmini & Kusenko 2000;
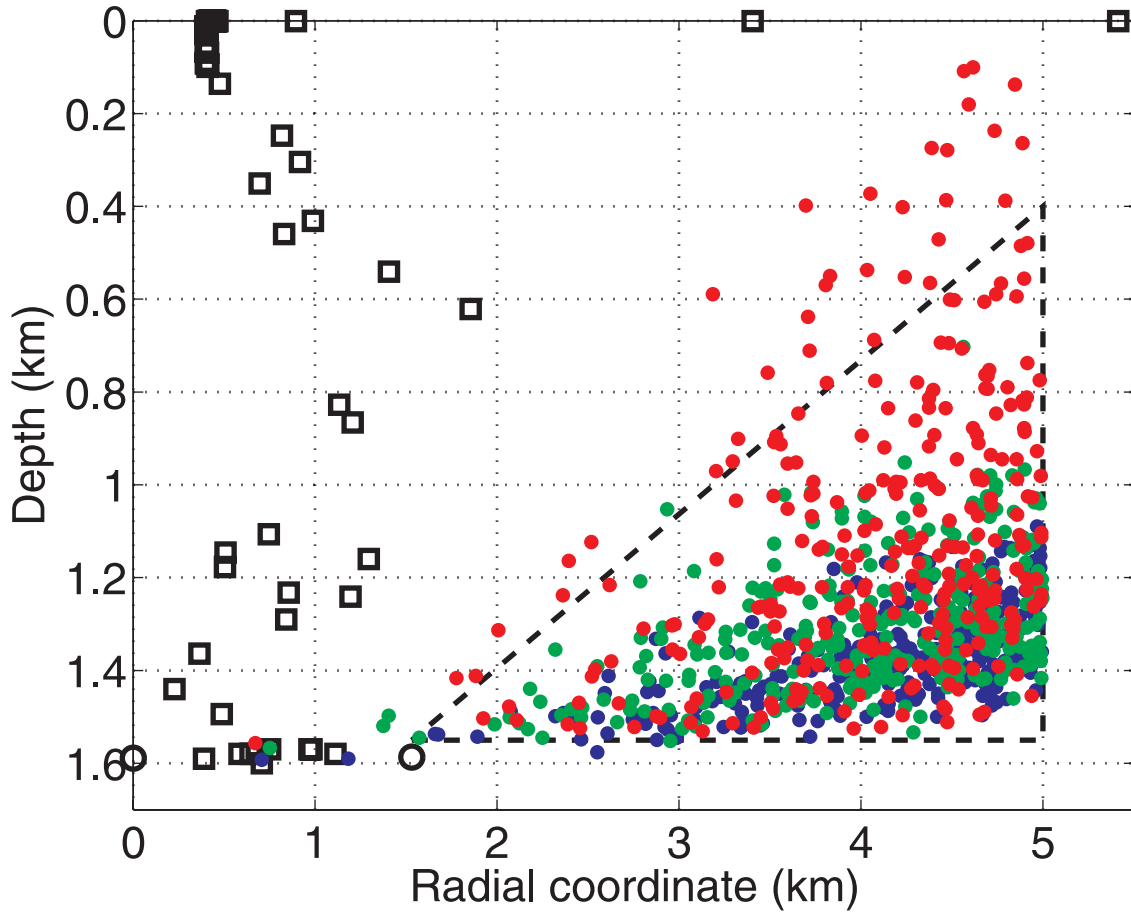
Fig. 14.—Side view of reconstructed positions (*squares*) for the 79 coincidences surviving all cuts except for fiducial volume. The event with greatest radial coordinate is that at 5.4 km (no events occur beyond the plot boundary). The fiducial volume is bounded by the dashed triangle. Circles represent hydrophone positions; 300 neutrino Monte Carlo events are also plotted, as colored dots, for each of three different energies, 10^{14} GeV (*blue*), 10^{15} GeV (*green*), and 10^{16} GeV (*red*).
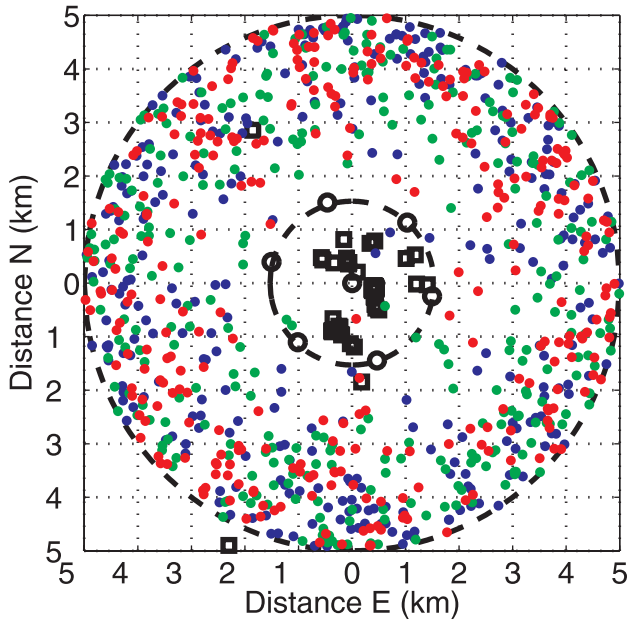

Fig. 15.—Top view of the reconstructed positions (*squares*) for the 79 acoustic neutrino candidates surviving the selection cuts. The fiducial volume is bounded by the two dashed circles. The small circles represent the positions of the hydrophones. Neutrino Monte Carlo events for three different energies are also shown with the same convention as in Fig. 14.
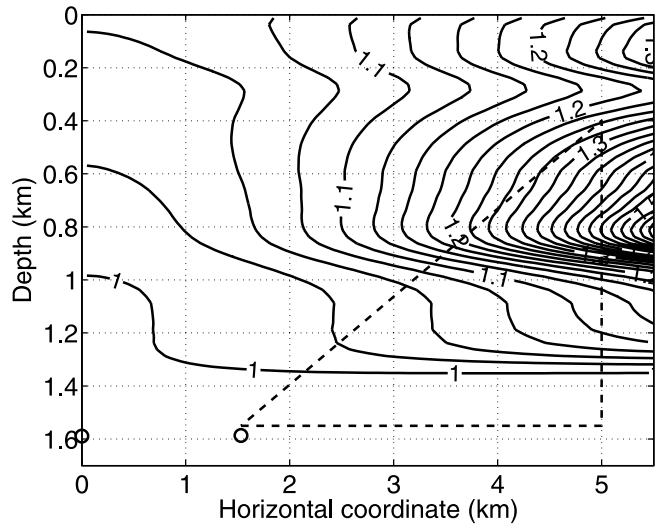

Fig. 16.—Degree of acoustic flux focusing at the central hydrophone, for sources at various points as calculated from ray tracing (Boyles 1984). Contours of equal focusing are given. The dashed curve encloses the fiducial volume used for the neutrino analysis. Central and peripheral hydrophone locations are indicated by circles. Factors >1 indicate focusing.
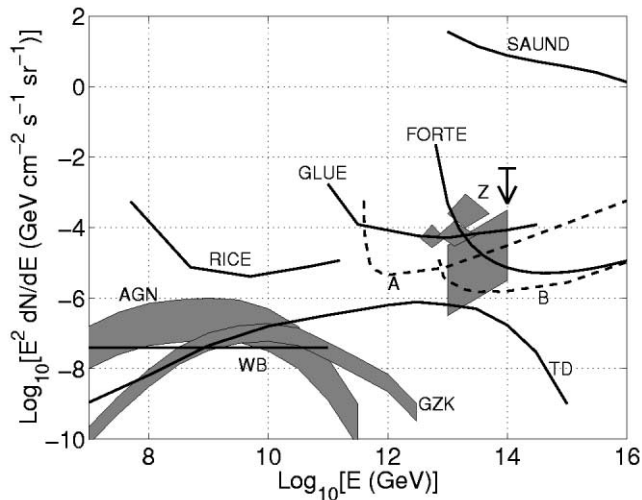
FIG. 17.—Diffuse neutrino flux limit from SAUND and other experiments and theoretical models of neutrino fluxes. The SAUND limit is the solid curve on the top right. The hypothetical sensitivities of two different optimized acoustic arrays (A and B), described in the text, are shown as dashed curves. Other experimental limits (*FORTE*, GLUE, and RICE) are shown in solid black. The remaining curves and regions indicate various theoretical models: Z for Z bursts (one large trapezoid, three small quadrilaterals, and arrow), TD for topological defects, AGN for active galactic nuclei, GZK for GZK neutrinos, and WB for the Waxmann-Bahcall limit.

Fodor et al. 2002; Waxman & Bahcall 1997; Hill & Schramm 1985; Sigl et al. 1999).

6. DISCUSSION

While the main motivation of this work has been to gain operational experience and investigate acoustic backgrounds for UHE neutrino detection, a flux measurement was obtained from the data. Although the limit, shown in Figure 17, is not competitive with the best limits (obtained with radio techniques), it represents the first UHE neutrino measurement performed with acoustic techniques. A wealth of information on noise conditions and the possible methods available to separate such noise from the neutrino signals has been obtained. Here we briefly discuss the characteristics of the SAUND array that turned out to be suboptimal for UHE neutrino detection, and we describe some of the properties that an optimized acoustic neutrino array should have.

The importance of calibrating the phase response of the acoustic array cannot be overstated. Without such a calibration, it is expected that the unknown phase properties of the readout will dominate the systematics of the measurement. An artificial source capable of providing acoustic signals similar to those from neutrinos with energies in the range considered here can be realized by discharging a capacitor in a column of sea water of length similar to that of a UHE shower. The instantaneous heating of the water should closely simulate the heating produced by showers, releasing an acoustic wave with the correct pancake geometry and phase/frequency structure.

The flatness of the acoustic radiation lobes from UHE showers is a crucial feature that allows noise rejection but also drastically limits the acceptance of SAUND. Refraction exacerbates the problem, by making regions of sea invisible to the array and by curving the emission pancake into a shape that often has little overlap with a planar hydrophone array. The planar geometry of the SAUND array is also poorly optimized to provide good position resolution in the direction orthogonal to the plane. The vertical resolution is estimated to be as poor as 400 m for

sources deeper than 1400 m, while it is 10 m for sources close to the surface. The resolution in the horizontal plane, however, is better than 10 m in most of the volume. A hydrophone array on a three-dimensional lattice would provide substantially larger acceptance and superior pancake-shape identification.

Although the long attenuation length of sound in water allows for large (several hundred meters to several kilometers) horizontal spacing for an optimized neutrino detector, to overcome the flatness of the acoustic radiation an array with dense ($\sim$10 m) vertical spacing is necessary. Even better, the ideal array would consist not of strings of discrete modules, but of strings sensitive to acoustic signals uniformly along their entire length. Such a detector element is not inconceivable and could perhaps be realized with a tube of fluid of sound speed different from the surrounding water, attached to hydrophones on each end. When an acoustic signal intercepts the tube, the difference in sound speeds leads to a signal propagating in both directions along the tube. The difference in arrival times at the two hydrophones could be used to localize the intersection point. Other possibilities may include interferometers built with an optical fiber running along the length of the string (although is it not clear how this could vertically localize signals).

To explore the possible sensitivity of an array of such strings with dense vertical spacing, two hypothetical arrays were tested with Monte Carlo neutrinos. Both are hexagonal lattices of 367 1.5 km long strings. The first (A) has 500 m nearest neighbor spacing and is bounded by a circle of radius $R = 5$ km drawn about the central string. The second (B) has 5 km spacing and is bounded by an $R = 50$ km circle. Both are taken to have a fiducial volume given by a cylinder of height 1.5 km and radius $R + 5$ km. Circles of various radii representing acoustic radiation from neutrinos of various energies were generated throughout this fiducial volume, with zenith from 0 to $\pi/2$. The calculated sensitivity of these arrays, requiring five strings to be hit, is given in Figure 17.

While water is the first medium to be tested for acoustic neutrino detection, salt (available in naturally occurring multi-km^3 underground domes) and ice (available near the poles in multi-km deep sheets) may be more favorable. In polar ice, as compared with ocean water, noise is expected to be significantly lower, and signals are predicted to be greater by an order of magnitude (Price 1996). It is possible that the hypothetical configurations A and B above, implemented in ice, possibly with more advanced triggering schemes in which thresholds are lowered for a time window after the first sensor is hit, may allow for better sensitivity at lower energy. Tests are necessary in these media to determine their merit. In any case, acoustic detection could be employed in combination with radio and optical Cerenkov techniques to provide more complete information about the very rare events occurring at the highest energies.

REFERENCES

Abbasi, R. U., et al. 2004, Phys. Rev. Lett., 92, 151101
Alvarez-Muniz, J., & Zas, E. 1998, Phys. Lett. B, 434, 396
Askar'yan, G. A. 1957, Soviet J. At. Energy, 3, 921
Askar'yan, G. A., & Dolgoshein, B. A. 1977, Soviet Phys.–JETP Lett., 25, 213
Bahcall, J. N., & Waxman, E. 2003, Phys. Lett. B, 556, 1
Boyles, C. A. 1984, Acoustic Waveguides: Applications to Oceanic Science (New York: Wiley)
Elmore, W. C., & Heald, M. A. 1986, Physics of Waves (New York: Dover), 154
Fodor, Z., Katz, S. D., & Ringwald, A. 2002, J. High Energy Phys., 0206, 046
Gaitan, D. F., Crum, L. A., Church, C. C., & Roy, R. A. 1992, J. Acoust. Soc. Am., 91, 3166
Gandhi, R., et al. 1998, Phys. Rev. D, 58, 093009
Gelmini, G., & Kusenko, A. 2000, Phys. Rev. Lett., 84, 1378
Gorham, P. W., Herbert, C. L., Liewer, K. M., Naudet, C. J., Saltzberg, D., & Williams, D. 2004, Phys. Rev. Lett., 93, 041101
Greisen, K. 1966, Phys. Rev. Lett., 16, 748
Heard, G. J., et al. 1997, in IEEE Conf. Proc. 2, OCEANS '97 (Fort Lauderdale: IEEE), 755
Hill, C. T., & Schramm, D. N. 1985, Phys. Rev. D, 31, 564
Hogg, R. V., & Craig, A. T. 1995, Introduction to Mathematical Statistics (5th ed.; Englewood Cliffs: Prentice Hall)
Keller, J. B., & Kolodner, I. I. 1956, J. Appl. Phys., 27, 1152
Keller, J. B., & Miksis, M. 1980, J. Acoust. Soc. Am., 68, 628
Knudsen, V. O., Alford, R. S., & Emling, J. W. 1948, J. Marine Res., 7, 410
Kravchenko, I., et al. 2003, Astropart. Phys., 20, 195
Kwiecinski, J., Martin, A. D., & Statso, A. M. 1999, Phys. Rev. D, 59, 093002
Landau, L. D., & Pomeranchuk, I. 1953, Dokl. Akad. Nauk USSR, 92, 535
———. 1953, Dokl. Akad. Nauk USSR, 92, 735
Learned, J. G. 1979, Phys. Rev. D, 19, 3293
Lehtinen, N. G., Adam, S., Gratta, G., Berger, T. K., & Buckingham, M. J. 2002, Astropart. Phys., 17, 279
———. 2004, Phys. Rev. D, 69, 013008
Migdal, A. B. 1956, Phys. Rev., 103, 1811
———. 1957, Soviet Phys.–JETP Lett., 5, 527
Price, P. B. 1996, Astropart. Phys., 5, 43
Sigl, G., Lee, S., Bhattacharjee, P., & Yoshida, S. 1999, Phys. Rev. D, 59, 043504
Spiesberger, J. L. 2001, J. Acoust. Soc. Am., 109, 3076
Sulak, L., et al. 1979, Nucl. Instrum. Methods Phys. Res., 161, 203
Takeda, M., et al. 1999, ApJ, 522, 225
Waxman, E., & Bahcall, J. N. 1997, Phys. Rev. Lett., 78, 2292
Weiler, T. J. 2001, in AIP Conf. Proc. 579, Radio Detection of High Energy Particles, ed. D. Saltzberg & P. Gorham (Melville: AIP), 58
Zatsepin, G. T., & Kuzmin, V. A. 1966, Soviet Phys.–JETP Lett., 4, 78